ZKG INTERNATIONAL
ISSN / eISSN 2366-1313
Publisher BAUVERLAG BV GMBH,
AVENWEDDER STR 55, GUTERSLOH, GERMANY, 33311
Volume 25-Issue 1-(2025)
https://doi.org/10.63386/618383

Turbulent combustion evolution of premixed hydrogen due to inherent instability and development space

Ao Zhang
College of Mechanical and Energy Engineering, Beijing University of Technology, Beijing, China, 100124;

Email: zhangaobj@163.com (Corresponding author)

Abstract

Laminar combustion of hydrogen in a premixed state has the potential to transition into turbulent combustion. The results demonstrate that the hydrogen premixed flame exhibits self-acceleration, progressing through the laminar combustion phase, followed by a transitional combustion phase, and ultimately transforming into a turbulent combustion phase. These flame characteristics, including flame propagation velocity, flame pulsation, perturbation length, and flame thickness, all exhibit consistent three-phase behaviors. The turning points, referred to as the critical radii R_{cr1} and R_{cr2}., mark the transition between different combustion phases. As the flame radius increases, the instability within the flame becomes more pronounced. When the radius exceeds R_{cr1}, spatial constraints due to wall reflections begin to influence the flame's development, altering the combustion dynamics. This phenomenon occurs as pressure waves are reflected by the walls, leading to alterations in the flow field within the combustion region, which ultimately influences the combustion parameters of the flame. In comparison, Conversely, a 30% increase in vessel volume leads to relatively minor variations in flame parameters. In instances of reduced space, the parameter that exhibits the greatest change is the heat release rate (HRR), which increases by 6.8%. Conversely, in the context of an enlarged space, the parameter that changes most significantly is the velocity, which decreases by 5.7%.

Keywords: Hydrogen; Premixed flame; Inherent instability; HRR; Turbulent combustion.

0. Introduction

Hydrogen is a renewable energy carrier known for energy efficiency and emissions reduction, making it a central research focus in both domestic and international research concerning automotive fuels [1]. Hydrogen can be generated through various methods, contributing to its versatility as an energy source [2]. Recent years have witnessed a concerted effort to promote low-carbon and zero-carbon alternatives within the internal combustion engine sector [3, 4]. Hydrogen provides several benefits, such as rapid flame propagation, a high calorific value, and a wide flammability range, all of which contribute to significantly improving combustion efficiency and enhancing thermal performance in internal combustion engines [5-7]. Internal combustion engines fueled by gas are often subjected to combustion cycle variations, primarily attributed to turbulence impacting flame propagation [8]. Consequently, investigating the transition characteristics of premixed flames from laminar combustion to turbulent combustion holds significant importance for the optimization of the combustion processes within engines.

Significant research has been conducted on laminar premixed combustion of hydrogen [9, 10]. The various modes of flame front instabilities, arising from both internal and external factors, are critical determinants influencing the propagation of laminar premixed flames. In the context of premixed combustion, flame instabilities frequently arise, distorting the flame fronts and exacerbating their wrinkling. Space-induced pressure fluctuations significantly affect flame stability, especially when confined spaces amplify the Darrieus-Landau (DL) instability. Increased pressure from localized disturbances shortens the instability's wavelength, enhancing flame wrinkling and accelerating propagation. These effects become more prominent as pressure waves interact with the flame, altering its dynamics, particularly in turbulent conditions[11, 12]. The diffusive thermal (DT) instabilities play a crucial role in enhancing the instability of hydrogen premixed flames, especially in lean mixtures. The low Lewis number of hydrogen causes differential diffusion, amplifying small perturbations and accelerating flame speed. Recent Direct Numerical Simulations (DNS) of turbulent hydrogen flames have shown that these instabilities, when combined with turbulence, significantly increase the turbulent flame speed by promoting larger flame surface areas and enhancing local reactivity [13]. This synergistic interaction leads to more complex flame structures and faster combustion, with distinct features like tongue-like structures at the flame front. Such phenomena can enhance flame propagation rates, potentially resulting in self-induced turbulence or deflagration. The enhanced velocity of flame propagation is attributed to the rapid expansion of the flame front area, facilitated by the cellular structure inherent to the flame. This process is referred to as flame self-acceleration [14, 15]. Extensive research has been devoted to flame self-acceleration resulting from inherent instabilities, often neglecting the influence of turbulence [15-17]. Kwon et al. [18] conducted investigations on $H_2/O_2/N_2$ flames within a dual-chamber vessel under constant high pressure, achieving pressures as high as 1.5 MPa. They observed that the acceleration exponent ranges between 1.23 and 1.36 depending on the equivalence ratios employed. In the process of turbulent premixed flame propagation, self-accelerating behavior is also evident. Flame self-acceleration, driven by inherent instabilities, facilitates the development of cellular structures within the flame fronts. Moreover, the influence of turbulence promotes the formation of cellular structures, augmenting the flame front area and further accelerating its propagation.

MacArt et al. [19] discovered that for spherical flames, distortions of the flame front induced by DT and hydrodynamic DL instabilities enhance reactant consumption, increase the heat release rate (HRR), and accelerate the flame propagation velocity. The propagation characteristics of turbulent premixed flames are influenced by two mechanisms: the generation and dissipation of wrinkles in the flame front [20]. The DL instability is widespread and consistently induces instability in flames. Conversely, the diffusive thermal instability can exhibit either stable or unstable behavior, contingent upon the effective Lewis number influencing the instability behavior. The Lewis number significantly influences flame instabilities, as evidenced by recent experiments involving lean-burning hydrogen and hydrogen-containing fuel mixtures [21-26], and it has been studied in recent direct numerical simulation [27-29]. When the Lewis number falls below the critical threshold ($Le = 1$), the diffusive thermal instability manifests instability characteristics [14]. I In both laminar and turbulent environments, the scale of wrinkles is typically two orders of magnitude larger than the flame thickness. Consequently, the characteristic wrinkles resulting from DL instability can predominantly develop in large-scale flames [30]. Mohan et al. [31] f observed that, under low to moderate turbulence intensities, the self-accelerating propagation of flames is primarily driven by inherent instabilities within the flame. Furthermore, as velocity fluctuations increase, the instability of the flame fronts becomes more pronounced. Lamioni et al. [32] demonstrated that wrinkles in the flame fronts induced by DL instability enhance the turbulence propagation velocity and induce positive strain rates at the negative curvature of the flame front. Liu et al. [33] found that at elevated Peclet numbers, cellular structures become predominant in the flame fronts. This dominance is attributed to the DL instability within the flame fronts, which fosters local instabilities. Dinesh et al. [34] noted that DL instability exhibits relative insensitivity to equivalence ratios, in contrast to the strong dependence of DT instability on these ratios. Thus, whether in laminar or turbulent conditions, the inherent instabilities of flames significantly impact their propagation behavior.

Space-induced pressure fluctuations play a crucial role in altering the hydrodynamic stability of premixed flames. As pressure increases due to localized disturbances, the flame front becomes more susceptible to DL instability, with shorter wavelengths of instability being amplified. This results in increased flame wrinkling and more pronounced instability, particularly in turbulent conditions. These effects become more significant as pressure waves propagate through the flame, causing the flame structure to evolve in response to dynamic pressure variations[35]. Mandilas et al. [36], Hu et al. [37] investigated the laminar combustion velocities of methane/hydrogen mixtures in cylindrical combustion chambers, examining different hydrogen volume fractions using the schlieren photographic method. Previous studies have reported laminar combustion velocities in small-volume vessels (5L [37, 38] and 3.5L [39]), which exhibit significant wall confinement effects and limited fields of view. Consequently, researchers extrapolated data for flame radii up to 25 mm to mitigate the influence of pressure increases and wall constraints on their measurements.

Most prior research on flame wrinkles has predominantly focused on macroscopic phenomena, such as perturbation induced by inherent instabilities and the development of flame front cellular structures. Although flame instabilities (DL and DT instabilities) in hydrogen-air flames have been extensively studied individually, the quantitative interactions between these instabilities and the effect of spatial confinement conditions (such as vessel geometry and volume) on the dynamic evolution from laminar to turbulent flames remain insufficiently understood. Specifically, existing studies rarely quantify the critical radii and corresponding flame characteristics at the exact points of laminar-to-turbulent transition under varied confinement conditions. This study aims to systematically quantify critical flame radius thresholds (R_{cr1}, R_{cr2}) and flame parameter evolutions under varied spatial confinements, clarifying the physical mechanisms by which vessel geometry amplifies inherent flame instabilities during laminar-to-turbulent transition in hydrogen-air flames.

1. Basic theory of premixed combustion

The average flame radius R refers to the radius obtained by treating a spherical premixed flame as a standard sphere, which can be expressed mathematically in Eq. 2-1:

$$R = \sqrt{A/\Pi} \qquad 2\text{-}1$$

Where A represents the area of the projection surface of the spherical premixed flame.

The flame propagation velocity S_b denotes the speed at which the flame advances from the burned area to the unburned area, as calculated in Eq. 2-2:

$$S_b = \frac{dR}{dt} \qquad 2\text{-}2$$

Flame stretch rate (α) significantly affects the laminar flame speed by influencing species concentration and temperature gradients in both the preheating and reaction zones [40, 41]. The stretch rate crucial as it reflects the kinetic behavior of the flame front. Furthermore, spherical flame propagation enables controlled experiments with well-defined stretch rates and simpler flame structures [38, 42]. The flame stretch rate is typically defined as the logarithmic rate of change over time of the infinitesimal area elements on the flame front, as shown in Eq. 2-3:

$$\alpha = \frac{d(\ln A)}{dt} = \frac{1}{A}\frac{dA}{dt} = \frac{2}{R}S_b \qquad 2\text{-}3$$

The ignited and unignited zones are separated by an infinitely thin flame front, where the flame expands due to the discontinuous density changes. In the case of flame fronts stretched by positive curvature, the flow lines of the unburned reactant fluid diverge and deflect as they pass through the flame front, leading to an increased area between these lines and a decreased flow field velocity compared to the flame combustion velocity. This results in the flame front advancing in the direction of the unburned reactants. Conversely, for flame fronts stretched by negative curvature, the opposite conclusion applies. The thermal expansion ratio can be expressed as shown in Eq. 2-4:

$$\sigma = \frac{\rho_u}{\rho_b} \qquad 2\text{-}4$$

Where: ρ_b represents the density of the burned zone and ρ_u represents the density of the unburned zone.

The Markstein length is a parameter commonly used to characterize the sensitivity of flame propagation velocity to the flame stretch rate. After the flame is no longer influenced by ignition and prior to the formation of cellular structures, the flame propagation velocity exhibits a clear linear relationship with the stretch rate α. This linear correlation has been previously established by researchers through theoretical analysis, numerical calculations, and experimental methods [34], and the specific expression can be stated as shown in Eq. 2-5:

$$S_{b,0} - S_b = L_b\alpha \qquad 2\text{-}5$$

The Reynolds number Re is a dimensionless parameter that characterizes flames in both laminar and turbulent combustion. The calculation formula for the flame Reynolds number during combustion can be expressed as shown in Eq. 2-6:

$$Re = \frac{ul}{\vartheta} \qquad 2\text{-}6$$

Where u denotes the average velocity of the flow field within the flame. This approach is predicated on the assumption that the average velocity provides a representative measure of the turbulent flow characteristics within the flame, thus enabling a more accurate assessment of the flow regime. The use of average velocity is particularly pertinent for simulating turbulent combustion, as it captures the integral effects of fluctuating velocities across both time and space, offering insights into the dominant flow phenomena that influence flame behavior. The equivalent diameter of the flame l and the kinematic viscosity ϑ are also included in this context.

- **i) Laminar combustion phase:** Smooth flame front, minimal perturbation ($Re < 2300$).
- **ii) Transitional combustion phase:** Initiation and rapid growth of cellular structures ($2300 < Re < 4000$).
- **iii) Turbulent combustion phase:** Fully developed multi-scale cellular structures ($Re > 4000$).

During the flame's expansion process, the flame fronts experience significant stretch rates; however, the curvature of the fronts may not be prominent, as shown Fig. 1. Transforming the contour of the flame fronts from polar coordinates into a Cartesian coordinate system facilitates easier observation and allows for the representation of localized flame characteristics. The local pulsation of the flame is defined as s, which quantifies the fluctuation of the flame pulsation radius R_θ relative to the average radius R, as expressed in Eq. 2-7:

$$s = R_\theta - R \qquad \text{2-7}$$

The total pulsating quantity refers to the integrated fluctuation of flame radius around its averaged spherical radius. To characterize the overall pulsation parameters of the flame, the total pulsation is obtained by integrating and resolving the pulsation at each angle, as described in Eq. 2-8:

$$S = \int_0^{2\Pi} \left| \frac{R_\theta + R_{\theta+d\theta}}{2} - R \right| d\theta \qquad \text{2-8}$$

Where S represents the total pulsation; s denotes the local pulsation at different angles; and R_θ is the radius at angle θ.

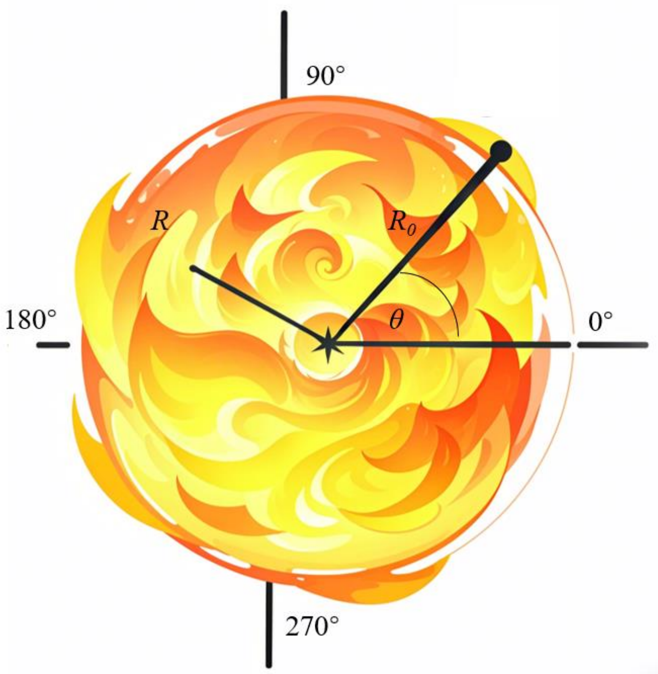

Fig. 1 Flame 2D schematic and definition of pulsation parameters

Spalding et al. [43] proposed a method to evaluate the laminar flame thickness by using the temperature difference $T_b - T_u$ on both sides of the flame surface, divided by the maximum temperature gradient, as expressed in Eq. 2-9:

$$\delta = \frac{T_b - T_u}{(dT/dx)_{max}} \qquad 2\text{-}9$$

Where T_b denotes the average temperature of the burned zone, and T_u signifies the average temperature of the unburned zone.

As the vortex pair interacts with the premixed flame, its vorticity is significantly influenced by the effects of dilatation and baroclinic torque, represented by the first two terms on the right side of Eq. 2-10. The sign of the baroclinic torque term depends on the misalignment between the density and pressure gradients within the flame, which can either reinforce or diminish the incoming vorticity through dilatation, leading to the creation of new vorticity. The contribution of the viscous term in Eq. 2-10 is typically minimal, leaving the baroclinic and dilatational terms as the primary mechanisms governing the dynamic behavior of the vorticity field.

$$\frac{\partial \omega}{\partial t} + u \cdot \nabla \omega = -\omega \cdot (\nabla \times u) + \frac{1}{\rho} \nabla p + \nu \nabla^2 \omega \qquad 2\text{-}10$$

Where, ω is the eddy vector, define as in Eq. 2-11, u is flow field velocity, ρ is the density, p is the pressure.

$$\omega = \nabla \times u = \begin{vmatrix} i & j & k \\ \frac{\partial}{\partial x_i} & \frac{\partial}{\partial x_j} & \frac{\partial}{\partial x_k} \\ u_i & u_j & u_k \end{vmatrix} = \left(\frac{\square u_k}{\square x_j} - \frac{\square u_j}{\square x_k}\right) i - \left(\frac{\square u_k}{\square x_i} - \frac{\square u_i}{\square x_k}\right) j + \left(\frac{\square u_j}{\square x_i} - \frac{\square u_i}{\square x_j}\right) k \qquad 2\text{-}11$$

2. Numerical simulation study of hydrogen premixed combustion

3.1 Geometric modelling

The fine meshes generated by the CONVERGE simulation software demonstrate excellent convergence and maintain precise dimensions of the model. Its Adaptive Mesh Refinement (AMR) and Highly Adaptive Mesh features effectively minimize errors in numerical simulations when dealing with moving boundaries [44]. A three-dimensional computational fluid dynamics (CFD) model was developed for a hydrogen constant volume bomb (CVB) using CONVERGE 3.0 software. The simulation area consisted of a cylinder with a diameter of d = 260 mm and height of l = 160 mm. The thermochemical conditions of the unburned gas are critical for combustion modeling. In this study, two cases were analyzed regarding hydrogen-air flames at two equivalence ratios: the first case with an equivalence ratio of 0.8 and the second case with an equivalence ratio of 1. This investigation examines the transition from laminar to turbulent combustion phases during hydrogen premixed combustion, analyzing flame instabilities and the impact of wall confinement on flame development.

The simulation configuration comprises boundary and initial conditions. The boundary conditions were set to simulate an open domain with zero-gradient conditions at the outlet, while the initial conditions were established based on the thermochemical state of the unburned gas mixture. Providing these details ensures an accurate representation of the physical phenomena within the simulated environment. Furthermore, the geometric modeling incorporates localized refinement, which refers to implementing a localized refinement technique in the computational grid to enhance the resolution of key flow features in the flame. This approach enhances the accuracy of the numerical results by allowing for a more detailed representation of critical regions within the simulation. One method involves local fixed refinement based on actual conditions, utilizing a source/sink model to ignite the mixture with 0.015 J of energy, accompanied by a significant temperature gradient at the flame front, which is fixed with a 6-level spherical diameter of 10 mm. The other method is adaptive refinement, where the temperature, velocity, and pressure fields within the bomb exhibit significant changes during the hydrogen premixed flame development process. Consequently, 6-level adaptive refinement of the flow field inside the bomb was conducted, using temperature, velocity, and pressure as indexes. The employment of these two refinement methods saves computational resources while simultaneously improving computational accuracy.

3.2 Combustion and turbulence modelling

The combustion model employed in this study utilizes the SAGE (Species Advection via Gas Expansion) method within the CONVERGE framework, allowing for integration with detailed chemical reaction kinetics. Large eddy simulation (LES) techniques were utilized to accurately simulate the turbulent combustion of hydrogen flames.

The LES simulations employed the Dynamic Smagorinsky model for sub-grid scale turbulent velocity fluctuations.

During the initial laminar phase of flame propagation (Re < 2300), the computational mesh (minimum grid size ~0.0625 mm) was fine enough to explicitly resolve the flame thickness (~0.1 mm), thus effectively minimizing the influence of sub-grid scale (SGS) turbulence. At this stage, the Dynamic Smagorinsky SGS model naturally produced negligible SGS viscosities due to very low velocity fluctuations, ensuring a seamless transition from laminar to turbulent combustion. As the flame progressively transitioned into the turbulent regime (Re > 4000), the SGS turbulence model actively captured unresolved turbulent fluctuations, ensuring accurate modeling of flame-turbulence interactions free from numerical inconsistencies.

3.3 Algorithm analysis

The coupled pressure and velocity algorithm implemented in CONVERGE is based on the PISO (Pressure Implicit with Splitting of Operators) algorithm. The PISO algorithm begins with a prediction step to solve the momentum equations, followed by several iterations to solve the pressure equation, which serves to correct the momentum field. This iterative process continues until the desired accuracy is achieved, and it is executed in conjunction with the other transport equations [45]. The iterative momentum equation is represented in Eq. 3-1:

$$\frac{\rho^n \mu_i^*}{dt} - \frac{\rho^n \mu_i^n}{dt} = -\frac{\partial p^n}{\partial x_i} + H_i^* \qquad \text{3-1}$$

where H_i^* denotes the convection, diffusion and source terms, ρ^n 、 μ_i^* denote the computational results of the iterative steps, and * denotes the latest intermediate field value. Each additional * level indicates an increase in temporal accuracy, and n denotes the currently calculated character segment. Subsequently, evaluation, iteration and computation are performed. The final result is obtained by correction and solving.

3.4 Grid-independence and model validation

Schlieren imaging experiments used for validation were performed in a cylindrical constant-volume chamber, identical in geometry to numerical setup. These experimental results are adopted from our previous study. Schlieren images used for validation were obtained from our previous experimental study conducted under identical cylindrical constant-volume conditions, with a diameter of 260 mm and height of 160 mm, at atmospheric initial pressure and temperature conditions, using high-speed imaging at 10000 fps [46]. Fig. 2(a) presents the schlieren diagram illustrating the development of a hydrogen premixed flame with radii of 10, 20, 30, 40, and 50 mm, captured using a high-speed digital camera at an equivalence ratio of 0.8. The fundamental grid sizes of 2, 4, and 8 mm were employed in the simulations as depicted in **Error! Reference source not found.**(b). and the results of laminar flame radius calculations under the three basic grid sizes were compared with the experimental data. The results show that the error between the simulation results and the experimental results of the three grid sizes is between 10%, but the 4mm grid is closer to the experimental results. So, basic size was selected to be 4 mm, taking into account the accuracy of the calculations and the low cost of the time.

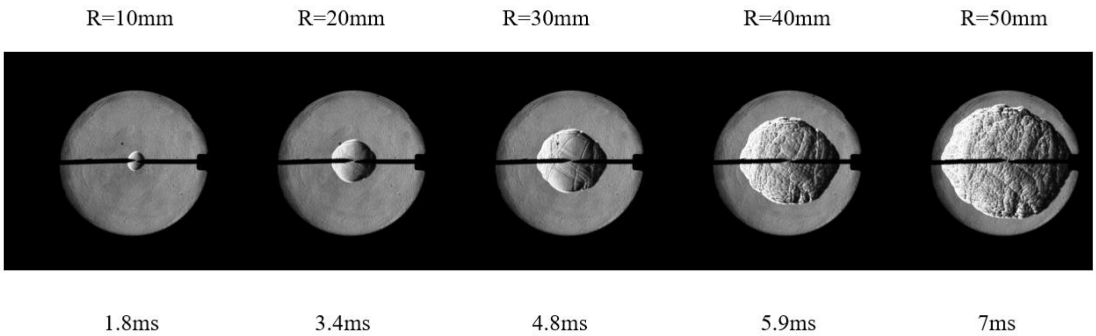

(a) Optical test results

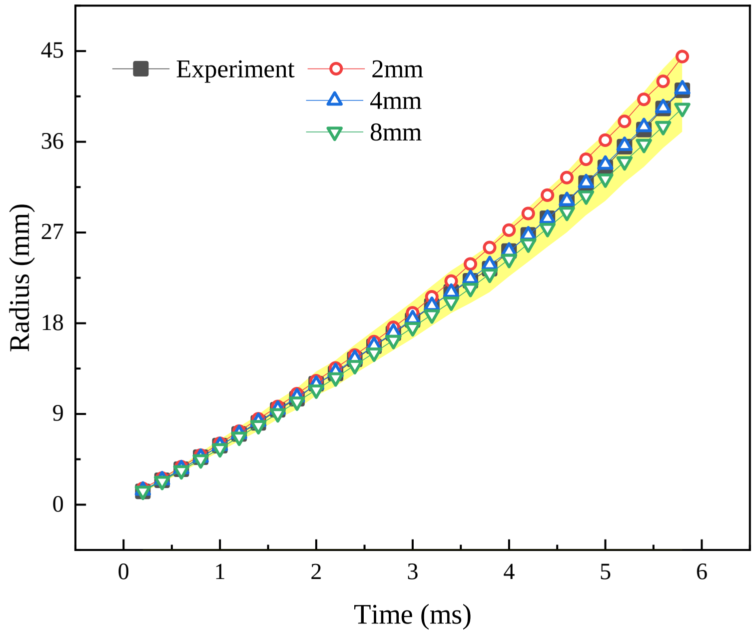

(b) Grid-independent verification

Fig. 2 Model verification

4. Results and analyses

4.1 Flame development process

Fig. 3 illustrates the various phases of flame evolution, categorized based on the radius of the expanding flame and the corresponding Reynolds number. This classification provides a detailed understanding of flame dynamics under different flow conditions. The phases depicted in Fig. 3(a) correspond directly to those in Fig. 3(b), each representing unique flame characteristics observed during the simulations. The Reynolds number evolution can be divided into three distinct phases: the initial laminar combustion phase, the intermediate transitional combustion phase, and the final turbulent combustion phase.

In the initial laminar combustion phase, the premixed flame expands outward, typically exhibiting a smooth spherical shape interspersed with isolated large flame front perturbations. During the transitional combustion phase, these large flame front perturbations begin to fragment into smaller ones, which further evolve into closed cellular structures. In the turbulent combustion phase, the larger cells subdivide into smaller ones. Once the cells reach a sufficiently small size, they cease to split and instead continue to grow with the increasing radius.

A comparative analysis of flames at equivalence ratios of 0.8 and 1.0 reveals that a lower equivalence ratio corresponds to a smaller Reynolds number under similar radii conditions. This indicates that lower equivalence ratios result in reduced combustion intensity, making the flame less likely to transition into the turbulent combustion phase. Conversely, lower equivalence ratios also lead to a higher density of wrinkles in the premixed flame fronts, exacerbating flame instabilities. In an ideal scenario, devoid of inherent instabilities and external disturbances, the spherical flame would propagate uniformly from the ignition center, maintaining a standardized spherical shape throughout its expansion.

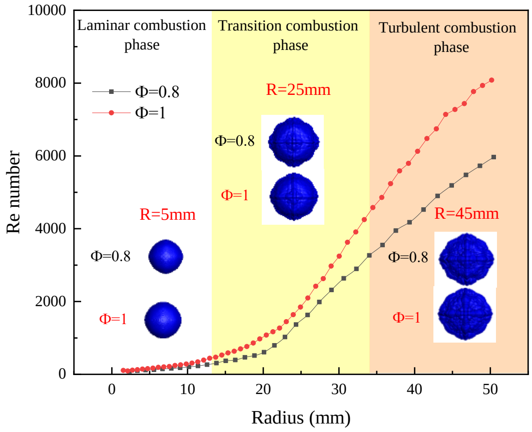

(a) Flame Reynolds number development law

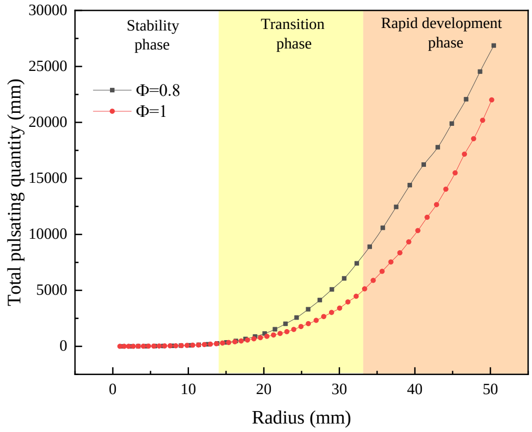

(b) Total flame pulsation development law

Fig. 3 Flame development law at different equivalent ratios

The flame propagation velocity is a crucial parameter for characterizing flame development, as it provides insight into the intensity of this process. As illustrated in Fig. 4, the trend in flame propagation velocity is consistent across the two conditions evaluated. Specifically, the flame propagation velocity at an equivalence ratio of 1 is higher than that at an equivalence ratio of 0.8. This velocity can be categorized into three distinct phases: the slow acceleration phase, the rapid acceleration phase, and the saturation acceleration phase. We denote the radii corresponding to the turning points within these phases as R_{cr1} and R_{cr2}. The first critical radius, R_{cr1}, is defined as the radius at which the flame propagation velocity begins to increase rapidly, while the second critical radius, R_{cr2}, marks the transition point where the flame propagation velocity stabilizes.

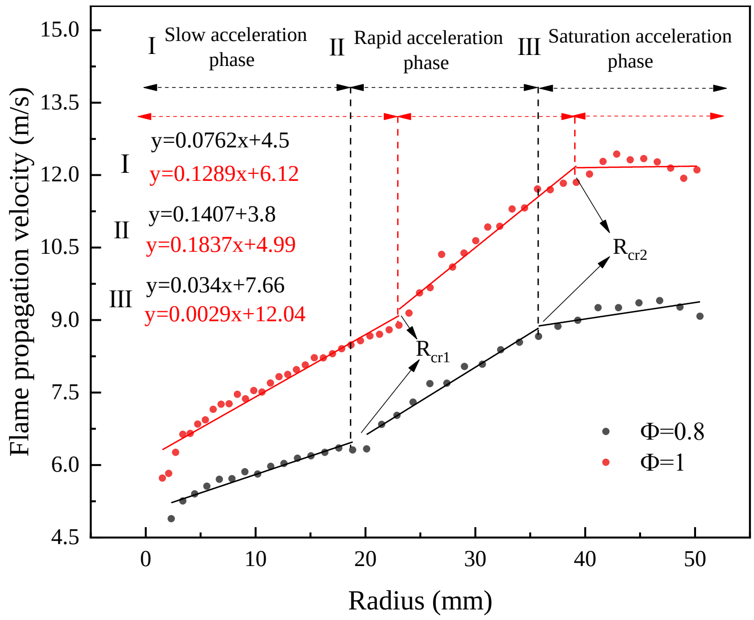

Fig. 4. Flame propagation velocity

The flame propagation velocity for the three phases was fitted using a linear regression analysis, and the resulting slopes (*K*) are presented in Table 1. Notably, the slope for the second phase is the largest, indicating that the flame propagation velocity increases the most rapidly during this stage. In contrast, the slope for the third phase is essentially zero, demonstrating that the flame propagation velocity remains relatively constant throughout this phase.

Table 1 Slopes of the three-phases *K* at different equivalence ratios

Equivalence ratio Φ	K_1	K_2	K_3
0.8	0.0762	0.1407	0.034
1	0.1289	0.1837	0.0029

To investigate the cause of self-acceleration during flame propagation, we examined the change in internal temperature of the flame as the radius develops, as illustrated in Fig. 5a. The flame temperature directly affects the combustion process and the thermodynamic properties of the flame. A higher flame temperature results in a greater temperature gradient with the unburned region, facilitating heat transfer to the surroundings and suppressing local instabilities through thermal conduction. Consequently, premixed flames with an equivalence ratio of 1 exhibit greater stability than those with an equivalence ratio of 0.8. Due to the influence of ignition energy, the initial combustion temperature of the flame is unstable. As the flame radius gradually increases, the effects of ignition energy on flame temperature become negligible, which we define as the ignition influence phase. With the increase in radius, the flame temperature progressively increases, accelerating the rate of chemical reactions and, ultimately, enhancing the flame propagation speed. This phenomenon also explains the observed slow acceleration of flame propagation during periods of steady combustion. In this stage, the flame fronts are generally smooth, with occasional large flame front perturbations appearing locally, without further fragmentation; we refer to this as the stable combustion phase. As the flame radius continues to develop, thermal diffusion stabilizes, and the combustion temperature levels off, with the turning point aligning with the first critical radius, R_{cr1}, defined in our previous study. Once the radius exceeds R_{cr1}, the fissures on the premixed flame fronts begin to develop rapidly, leading to the formation of cellular structures. This occurs because, when the flame radius exceeds Rcr1, the smaller flame stretch rate can no longer maintain the original shape of the flame, resulting in unstable development of the flame fronts, which we classify as the perturbations and cell phase.

The density-weighted flame velocity serves as a parameter that represents the efficiency of the combustion reaction of the fuel mixture. As shown in Fig. 5b, the fuel consumption for the development of the premixed flame varies with the flame propagation velocity and follows a three-phase trend: a slow accelerating combustion phase, a rapid accelerating combustion phase, and a saturation combustion phase. The consumption rate of the mixture at an equivalence ratio of 1 is greater than that at an equivalence ratio of 0.8, indicating that the combustion reaction rate of the flame is faster. This also corroborates the observation that the combustion temperature within the flame is higher for an equivalence ratio of 1, as illustrated in Fig. 5a.

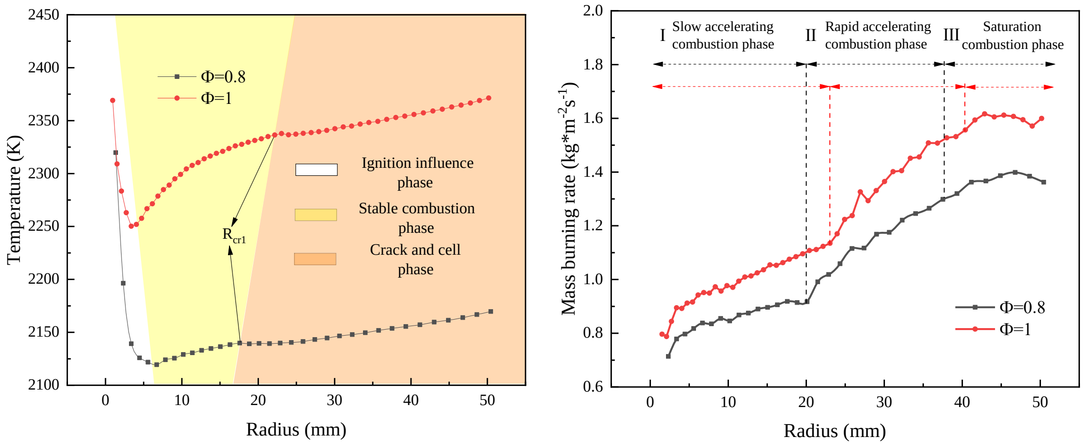

(a) Temperature change inside the flame (b) Mass burning rate

Fig. 5 Flame development parameters

The Markstein length is a critical parameter used to quantify the influence of flame stretch rate on flame propagation velocity and to analyze its effect on the burning rate of unstretched laminar flow flames [47, 48]. Fig. 6 illustrates the relationship between flame propagation velocity and stretch rate at various equivalence ratios. The data reveal that the evolution of flame propagation velocity with respect to stretch rate can be categorized into three distinct phases: the ignition influence phase, the stable combustion phase, and the flame cell phase. By excluding the flame cell and ignition influence phases, the resulting curves were fitted to determine the Markstein lengths of 0.441 and 0.772 for the two operating conditions. The analysis demonstrates that flame propagation velocity is inversely related to stretch rate. When flame fronts exhibit bulging due to elevated local stretch rates, the propagation velocity decreases, which in turn mitigates further deformation of the flame fronts, thereby contributing to flame stability.

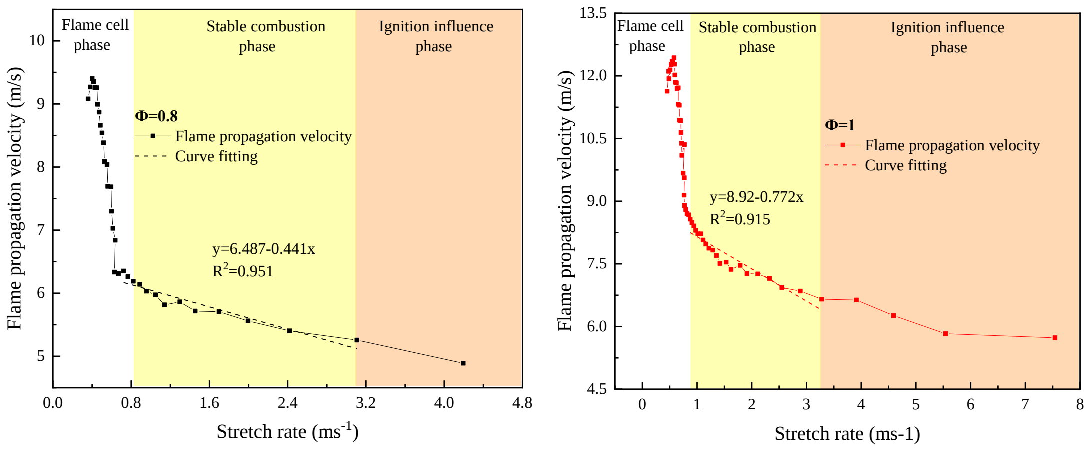

Fig. 6. Variation of flame propagation velocity with flame stretch rate

To eliminate the influence of increased chemical reactivity, we present the normalized flame speed ($\overline{S_b} = \frac{S_b}{S_{b,0}}$) curve. Since the same chemical reactivity affects both stretched and unstretched flames, it can be assumed that the effects of chemical reactivity are balanced [17]. As illustrated in Figure 7, the large flame stretch rate during the initial phase constrains the development of flame speed, resulting in a $\overline{S_b}$ value of less than 1. In this phase, the influence of flame stretch rate on $\overline{S_b}$ is predominant. As the flame radius increases, the stretch rate gradually decreases, allowing the effects of the stretch rate to become negligible. At this stage, flame acceleration becomes increasingly governed by the inherent instabilities of the flame.

At an equivalence ratio of 1 (Le=1), the effect of DT instability on the flame is neutral. The area corresponding to equivalence ratios below 1 in Figure 7 represents flame acceleration attributable solely to DL instability, which is not sensitive to changes in equivalence ratio [34]. It can then be inferred that the area between the two conditions reflects the acceleration of the flame due to DT instability. At an equivalence ratio of 1, the neutral effect of DT instability leads to minimal overall flame pulsation. Conversely, at an equivalence ratio of 0.8, thermal diffusion enhances flame instability, contributing to irregular premixed flame morphology. Figure 7 demonstrates that, under the present conditions, the impact of DL instability on the flame outweighs that of DT instability. The total shaded area represents the combined effects of both DT and DL instabilities on flame speed.

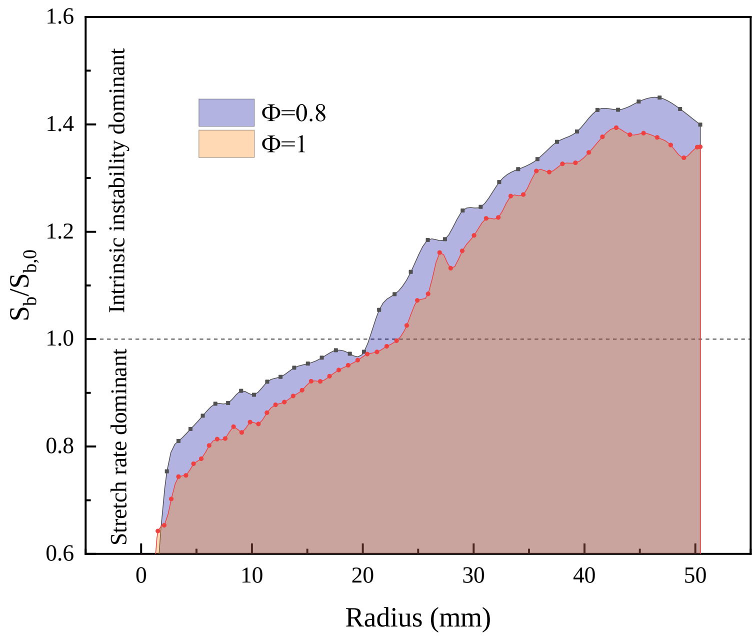

Fig. 7. Dimensionless flame velocity development with flame radii

4.2 Flame fronts development

Perturbations on the flame fronts arise and continuously grow, resulting from inherent instabilities that cannot be suppressed. The total flame front perturbation length L increases due to combined effects of perturbation extension and splitting into smaller cellular structures. In this context, 'perturbations on the flame fronts' refers to the irregularities and local deformations forming on the flame surface as it propagates, indicating flame instability. These perturbations serve as indicators of flame instability and are influenced by various factors, including turbulence and inherent flame instabilities. The expansion and stretching of flame perturbations at the flame fronts are key parameters reflecting the cellularity process of the flame.

During the early phase of flame propagation, inherent instabilities are minimal, allowing perturbations on the flame fronts to extend and evolve progressively with flame development. As the flame continues to evolve, larger perturbations split into smaller-scale perturbations, progressively developing into fully formed cellular structures. When perturbations neither expand nor split spontaneously, L increases proportionally with flame radius expansion, emphasizing the self-development characteristic of flame perturbations. Consequently, the slope of the growth rate of the total perturbations length L in relation to the flame radius R provides insight into the perturbations growth rate. By examining the physical quantity L, we can determine the stability of the spherical flame fronts with perturbations.

The perturbation evolution phases depicted in Fig. 8 closely align with the phases of flame development outlined in Fig. 3, categorized as follows:

i) **Initial Stable Perturbation Phase** (corresponding to the laminar combustion phase in Fig. 3): During this phase, the flame expands smoothly in a spherical shape or exhibits only a few stable large perturbations, as the flame radius increases, the expansion rate of the perturbation also rises.

ii) **Perturbation Development Phase** (corresponding to the transitional combustion phase in Fig. 3): In this stage, large perturbations begin splitting into smaller ones, indicating an increase in flame instability and a rapid growth in perturbation length.

iii) **Cellular Structure Growth Phase** (corresponding to the turbulent combustion phase in Fig. 3): As the flame radius continues to develop, smaller perturbation evolves into complex cellular structures, signaling a transition into a turbulent state, which results in further perturbation length increases.

In the initial stable perturbation phase, the flame maintains a predominantly spherical shape with minor perturbations. Owing to the high flame stretch rates, only large-scale perturbations are present on the flame fronts, growing as the radius expands. During the perturbations development phase, as flame stretch rates decrease, the flame fronts cannot maintain their original morphology, leading to the splitting of the perturbations, where large-scale perturbations progressively develop into small-scale ones. The growth rate of flame perturbation length accelerates during this period. In the cell growth phase, as flame radii further develop, the limiting effect of stretch rate on flame front perturbations caused by inherent flame instabilities diminishes. Perturbations of various scales rapidly emerge, accompanied by intensified mutual interactions, yielding a complex flame front structure. The continued evolution of small perturbations gradually forms closed cellular structures, while large-scale cells further divide into smaller cellular structures, ultimately resulting in an increase in perturbations length.

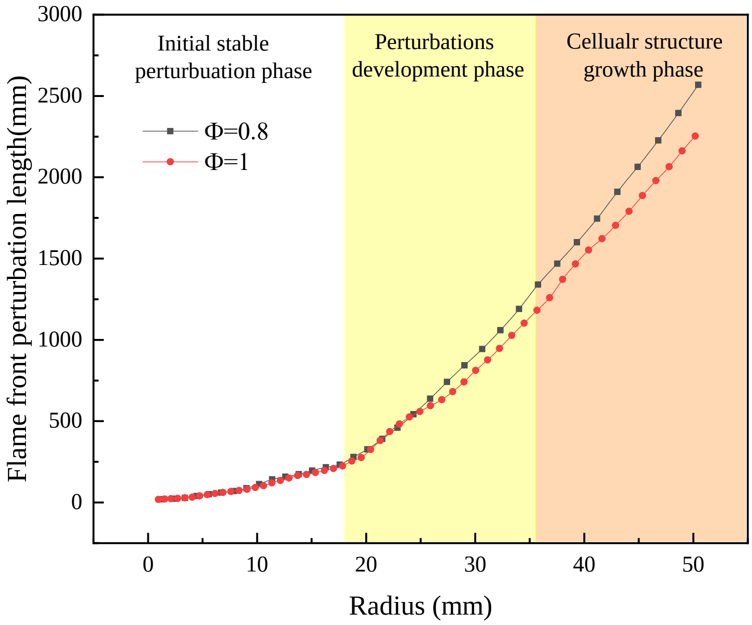

Fig. 8. Evolution of flame front perturbation length at different equivalence ratios

Fig. 9 illustrates the variation of vorticity within the flame structure under different operating conditions. This visualization is crucial for understanding the complex flow dynamics and turbulent characteristics that influence flame behavior. The analysis of vorticity provides essential insights into the interactions between the flame front and the surrounding flow field. Specifically, regions of high vorticity are associated with enhanced mixing processes, which lead to improved combustion efficiency. Additionally, fluctuations in vorticity can reveal important information about the stability and emission characteristics of the flame, underscoring the significance of turbulent intensity in combustion phenomena.

A thorough examination of these vorticity patterns is vital for advancing our understanding of flame stabilization mechanisms and for optimizing combustion systems in practical applications. As the flame develops, vorticity at the flame fronts gradually increases, resulting in enhanced turbulence intensity. This increase in turbulence intensity further promotes effective mixing of fuel and oxygen, creating more complex turbulent structures that facilitate efficient combustion. Consequently, this improves combustion efficiency, influences the dynamic behavior of the gases surrounding the flame, alters the shape and propagation of the flame, and ultimately affects flame stability.

Turbulence and combustion are interrelated processes. The heat generated by combustion affects the fluid properties, while variations in turbulent structure influence the rate and distribution of combustion. This interaction ultimately accelerates the combustion dynamics of the flame.

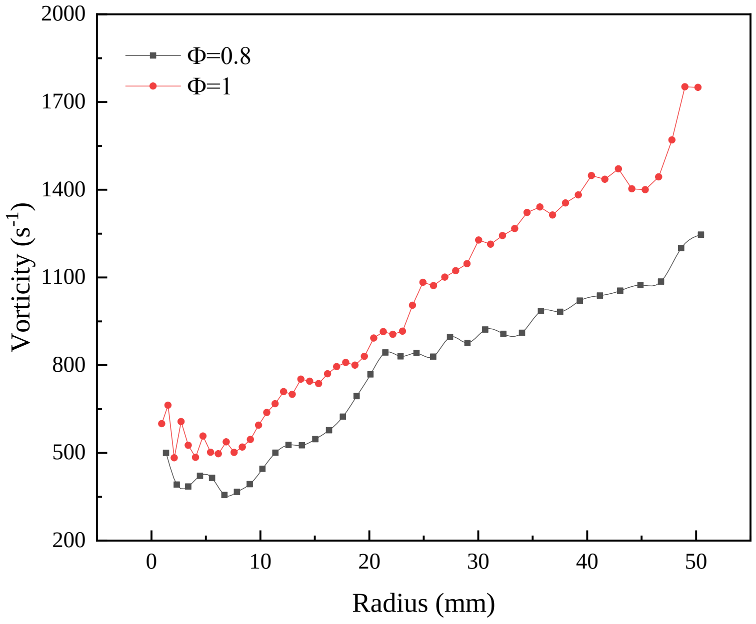

Fig. 9 Flame fronts vorticity change

The flame fronts serve as the primary reaction zone, characterized by elevated turbulent kinetic energy (TKE). This increase in TKE is attributed to the expansion of gases resulting from the heat generated during combustion, which subsequently leads to the formation of turbulent structures. The flame temperature significantly impacts flame stability, with the temperature of the flame fronts serving as an indicator of combustion intensity. The heat release rate (HRR) is a critical parameter for assessing the combustion efficiency of premixed flames, as it directly influences combustion conditions. Specifically, HRR quantifies the thermal energy released over time during combustion, which is essential for understanding flame performance. A higher HRR indicates a more efficient combustion process, resulting in improved energy output and reduced emissions.

As illustrated in Fig. 10, prior to reaching the critical radius R_{cr1} of the flame—18.5 mm for an equivalence ratio of 0.8 and 23 mm for an equivalence ratio of 1—parameters such as temperature, HRR, TKE, and density within the flame fronts remain relatively stable. However, once the flame radii surpass R_{cr1}, a notable transformation of the flame front parameters occurs. At this juncture, perturbation growth accelerates, leading to a sudden decline in the combustion parameters of the flame fronts. This behavior indicates that the flame exhibits an unstable characteristic, resulting in a diminished reaction state.

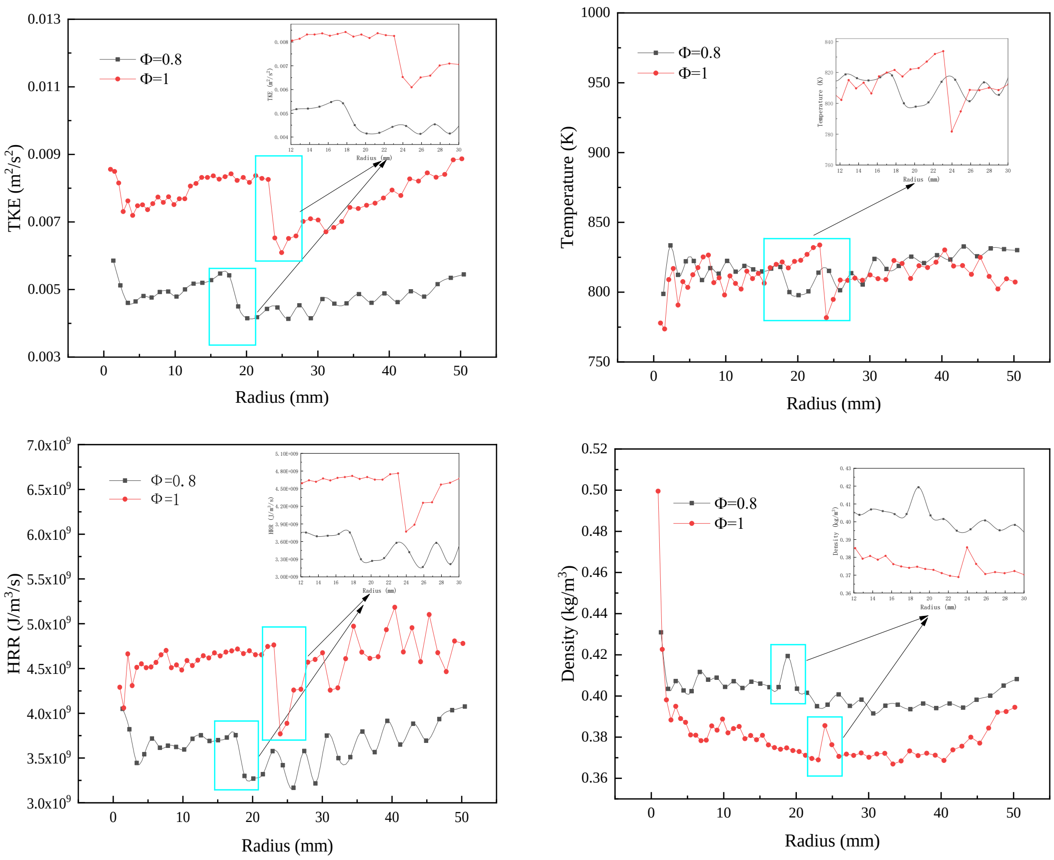

Fig. 10. Flame fronts HRR, TKE, Temperature, Density

The Fig. 11 shows the development of flame thickness with flame radii. The results indicate that the flame thickness at an equivalence ratio of 0.8 is greater than that observed at an equivalence ratio of 1, a finding that aligns with previous research. This observation suggests that as the equivalence ratio decreases, the associated flame dynamics become more complex, leading to variations in flame thickness. The implications of these variations highlight the need for further investigation into the underlying mechanisms that contribute to such differences in flame behavior. This is due to the fact that an equivalence ratio of 1 has a greater stretch rate for the same radii, and the greater stretch rate results in a greater force on the flame fronts, causing reduction in flame thickness. However, flame thickness does not remain constant during the development process. Similar to the conclusions from earlier in this paper, flame thickness development follows a three-phases developmental pattern. When $R < R_{cr1}$, the flame is in the stable laminar combustion phase, and the flame thickness is basically constant. At this time, the flame stretch rate is larger, the force of the flame fronts is larger, and the flame thickness is smaller. When $R > R_{cr1}$, the flame begins to become unstable and the flame develops at a higher constant acceleration. The smaller stretch rate makes the flame insufficient to continue to maintain a small flame thickness. At this point the flame thickness increases rapidly and then remains stable. When $R > R_{cr2}$, the cell division reaches its limit, cells no longer divide into smaller cells. At this time, the flame propagation acceleration begins to decrease, the burning speed of the flame slows down, and the flame thickness begins to decrease.

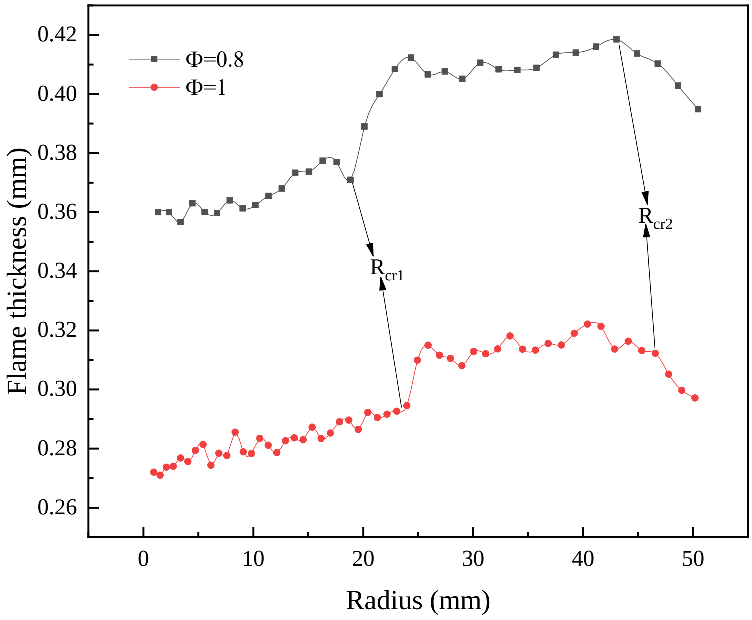

Fig. 11. Flame thickness change

4.3 Flame development under different perspectives and space

Fig. 12 illustrates the variation in flame propagation velocity at 0° and 90° under two conditions. The flame propagation velocities in these directions exhibit inconsistent behavior, particularly after the flame reaches the critical radius R_{cr1}, at which point this inconsistency becomes evident. In the 0° direction, the flame propagation velocity is notably higher. This is attributed to the larger distance from the wall, resulting in fewer disturbances from wall interactions. Consequently, the flame undergoes more vigorous changes in this direction.

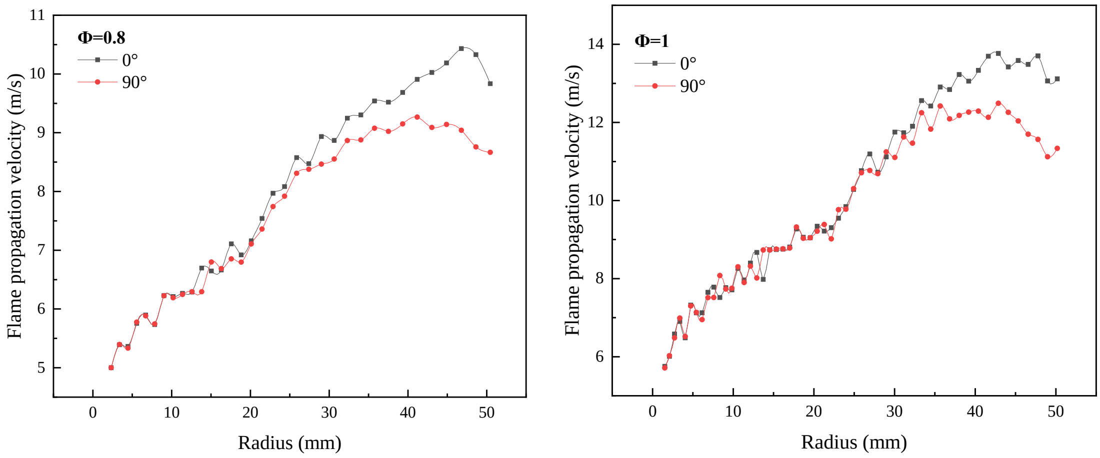

Fig. 12. Velocity of flame propagation in different directions

Fig. 12 clearly demonstrates that the flame front parameters exhibit inconsistency across different directions. To further quantify the deviations in these parameters during flame development, we compare the average values of the flame front parameters in various directions, as described in Eq. 4-1:

$$Deviation = \frac{\sum_{0^\circ} parameter}{\sum_{90^\circ} parameter} \quad \text{4-1}$$

Fig. 13 illustrates the average deviations of flame propagation velocity, turbulent kinetic energy (TKE), heat release rate (HRR), vorticity, and temperature during the development process under the two conditions analyzed. The deviations in these parameters are particularly pronounced for an equivalence ratio of 0.8, indicating a greater degree of instability in the flame. In both conditions, the velocity exhibits significant fluctuations, which can be attributed to the reflection of pressure waves by the wall. This reflection interacts with the flame, directly influencing its combustion state and resulting in changes to the local flow field velocity.

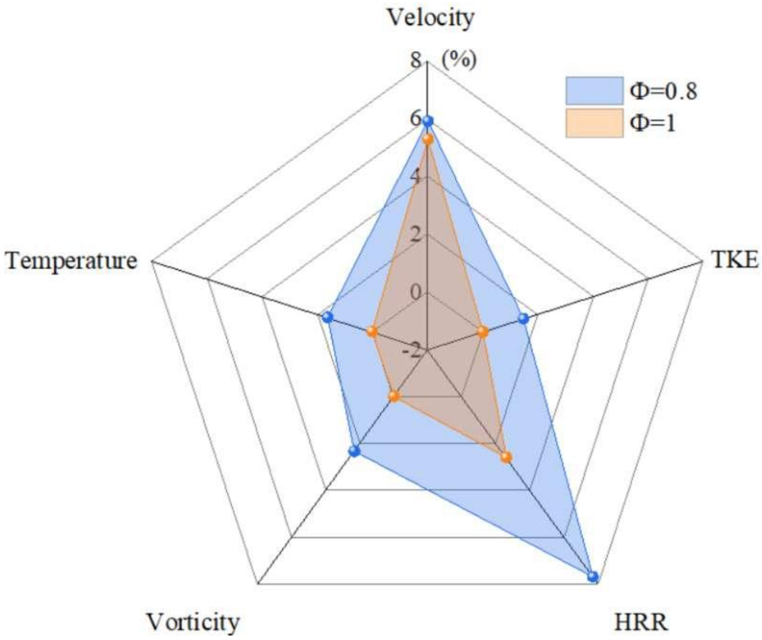

Fig. 13. Parameters deviation at different directions

Fig. 14a illustrates the variations in flame front parameters after magnifying and shrinking the constant volume bomb (CVB) space by 30%. It is evident that changes in the development space significantly impact the combustion parameters of the flame fronts, indicating that the development space constrains the flame's evolution. Specifically, in the case of a 30% reduction in space, the parameters most affected are the flame velocity, turbulent kinetic energy (TKE), and heat release rate (HRR), with HRR showing the most pronounced change. In contrast, expanding the space by 30% results in less significant variations in flame front parameters, with the most notable change occurring in velocity. This suggests that a smaller space yields more dramatic changes in flame parameters, subsequently affecting flame stability.

Fig. 14b depicts the deviations of parameters in different directions under varying spatial conditions. Notably, parameter changes are substantial during space reduction. The observed fluctuations in vorticity indicate that in confined spaces, the primary contributor to flame wrinkles is the increase in vorticity. Conversely, in larger spaces, both the HRR and vorticity decrease due to the heat transfer dynamics of the flame.

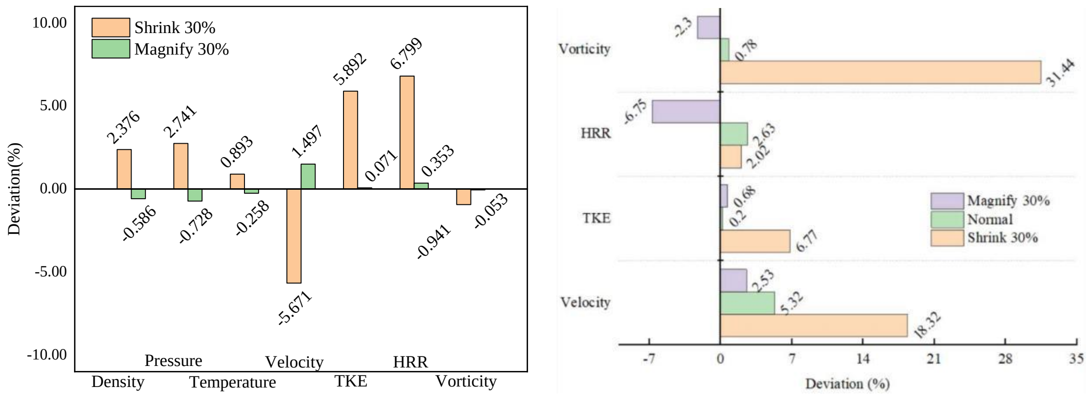

(a) Mean parameters deviation of flame fronts

(b) Parameters deviation at different direction of flame fronts

Fig. 14 Parameter deviation under different spaces

5. Conclusions

This study comprehensively examines the development process of hydrogen premixed flames under varying equivalent ratios and constant volume bomb (CVB) conditions through three-dimensional numerical simulations. Key conclusions are as follows:

1. The evolution of hydrogen premixed flames is categorized into three distinct phases: laminar, transitional, and turbulent combustion, with critical transition points identified as R_{cr1} and R_{cr2}. Parameters such as flame propagation velocity, mass burning rate, total pulsation, and perturbations length demonstrate this three-phase behavior.

2. Initially, higher stretch rates positively contribute to flame stability, leading to stable development primarily driven by increases in flame temperature. Beyond the critical radius R_{cr1}, inherent instabilities, particularly Darrieus–Landau (DL) instability, significantly affect flame acceleration and speed. This study emphasizes the dominant influence of DL instability over diffusive thermal (DT) instability on flame speed. Future studies should systematically investigate how Lewis number variations influence flame dynamics under diverse conditions, further elucidating the interactions between DL and DT instabilities in hydrogen premixed flames. Additionally, flame thickness evolution warrants further quantitative characterization regarding its dependence on flame radius and stretch rate.

3 Once exceeding the critical radius R_{cr1}, significant parameter variations appear across different spatial directions. Quantifying deviations in flame front parameters reveals pronounced fluctuations in velocity due to pressure wave reflections from walls, which interact with the flame and modify local flow field velocities. The CVB development space significantly influences these dynamics; for instance, a 30% reduction in space yields a 6.8% increase in heat release rate (HRR), while a 30% expansion leads to a 5.7% reduction in velocity. Notably, increased vorticity in confined spaces primarily contributes to flame wrinkles, whereas in larger spaces, HRR and vorticity decrease due to heat transfer dynamics.

References:

1. Tarasenko, A.B.; Kiseleva, S.V.; Popel, O.S., Hydrogen energy pilot introduction – Technology

competition. *Int J Hydrogen Energ* **2022**, 47, (23), 11991-11997.

2. Hassan, Q.; Abdulateef, A.M.; Hafedh, S.A.; Al-samari, A.; Abdulateef, J.; Sameen, A.Z.; Salman, H.M.; Al-Jiboory, A.K.; Wieteska, S.; Jaszczur, M., Renewable energy-to-green hydrogen: A review of main resources routes, processes and evaluation. *Int J Hydrogen Energ* **2023**, 48, (46), 17383-17408.
3. Li, M.; Wu, H.; Zhang, T.; Shen, B.; Zhang, Q.; Li, Z., A comprehensive review of pilot ignited high pressure direct injection natural gas engines: Factors affecting combustion, emissions and performance. *Renewable and Sustainable Energy Reviews* **2020**, 119, 109653.
4. Sun, Z.; Hong, J.; Zhang, T.; Sun, B.; Yang, B.; Lu, L.; Li, L.; Wu, K., Hydrogen engine operation strategies: Recent progress, industrialization challenges, and perspectives. *Int J Hydrogen Energ* **2023**, 48, (1), 366-392.
5. Teoh, Y.H.; How, H.G.; Le, T.D.; Nguyen, H.T.; Loo, D.L.; Rashid, T.; Sher, F., A review on production and implementation of hydrogen as a green fuel in internal combustion engines. *Fuel* **2023**, 333, 126525.
6. Shi, W.; Li, Z.; Dong, W.; Sun, P.; Yu, X.; Yang, S.; Li, J.; Qu, H.; Liu, Y.; Li, X.; Zhao, C.; He, Z.; Liu, M., Effect of pre-combustion chamber hydrogen injection strategy on emissions and fuel economy of jet ignition engines under ultra lean-burn conditions. *Int J Hydrogen Energ* **2025**, 113, 147-160.
7. Rodriguez Henao, D.C.; Zuluaga Castrillón, D.; Colorado, A.; Amell, A.A., Impact of hydrogen addition to natural gas mixtures in a premixed combustion system and heat transfer by infrared radiation. *Int J Hydrogen Energ* **2025**.
8. Vermorel, O.; Richard, S.; Colin, O.; Angelberger, C.; Benkenida, A.; Veynante, D., Towards the understanding of cyclic variability in a spark ignited engine using multi-cycle LES. *Combust Flame* **2009**, 156, (8), 1525-1541.
9. Hassan, M.I.; Aung, K.T.; Faeth, G.M., Measured and predicted properties of laminar premixed methane/air flames at various pressures. *Combust Flame* **1998**, 115, (4), 539-550.
10. Verhelst, S.; Woolley, R.; Lawes, M.; Sierens, R., Laminar and unstable burning velocities and Markstein lengths of hydrogen–air mixtures at engine-like conditions. *P Combust Inst* **2005**, 30, (1), 209-216.
11. Gaucherand, J.; Laera, D.; Schulze-Netzer, C.; Poinsot, T., DNS of Turbulent Premixed Ammonia/Hydrogen Flames: The Impact of Thermo-Diffusive Effects. *Flow, Turbulence and Combustion* **2024**, 112, (2), 587-614.
12. SIVASHINSKY, G.I., Diffusional-Thermal Theory of Cellular Flames. *Combust Sci Technol* **1977**, 15, (3-4), 137-145.
13. Berger, L.; Attili, A.; Pitsch, H., Synergistic interactions of thermodiffusive instabilities and turbulence in lean hydrogen flames. *Combust Flame* **2022**, 244, 112254.
14. Huo, J.; Saha, A.; Ren, Z.; Law, C.K., Self-acceleration and global pulsation in hydrodynamically unstable expanding laminar flames. *Combust Flame* **2018**, 194, 419-425.
15. Wu, F.; Jomaas, G.; Law, C.K., An experimental investigation on self-acceleration of cellular spherical flames. *P Combust Inst* **2013**, 34, (1), 937-945.
16. Kim, W.K.; Mogi, T.; Kuwana, K.; Dobashi, R., Self-similar propagation of expanding spherical flames in large scale gas explosions. *P Combust Inst* **2015**, 35, (2), 2051-2058.
17. Yang, S.; Saha, A.; Wu, F.; Law, C.K., Morphology and self-acceleration of expanding laminar flames with flame-front cellular instabilities. *Combust Flame* **2016**, 171, 112-118.

18. Kwon, O.C.; Rozenchan, G.; Law, C.K., Cellular instabilities and self-acceleration of outwardly propagating spherical flames. *P Combust Inst* **2002**, 29, (2), 1775-1783.
19. MacArt, J.F.; Wang, J.M.; Popov, P.P.; Freund, J.B., Detailed simulation of laser-induced ignition, spherical-flame acceleration, and the origins of hydrodynamic instability. *P Combust Inst* **2021**, 38, (2), 2341-2349.
20. Chaudhuri, S.; Wu, F.; Law, C.K., Scaling of turbulent flame speed for expanding flames with Markstein diffusion considerations. *Phys Rev E Stat Nonlin Soft Matter Phys* **2013**, 88, (3), 033005.
21. Cai, X.; Fan, Q.; Bai, X.; Wang, J.; Zhang, M.; Huang, Z.; Alden, M.; Li, Z., Turbulent burning velocity and its related statistics of ammonia-hydrogen-air jet flames at high Karlovitz number: Effect of differential diffusion. *P Combust Inst* **2023**, 39, (4), 4215-4226.
22. Lipatnikov, A.N.; Chen, Y.; Shy, S.S., An experimental study of the influence of Lewis number on turbulent flame speed at different pressures. *P Combust Inst* **2023**, 39, (2), 2339-2347.
23. Venkateswaran, P.; Marshall, A.; Shin, D.H.; Noble, D.; Seitzman, J.; Lieuwen, T., Measurements and analysis of turbulent consumption speeds of H2/CO mixtures. *Combust Flame* **2011**, 158, (8), 1602-1614.
24. Wang, S.; Elbaz, A.M.; Arab, O.Z.; Roberts, W.L., Turbulent flame speed measurement of NH3/H2/air and CH4/air flames and a numerical case study of NO emission in a constant volume combustion chamber (C.V.C.C.). *Fuel* **2023**, 332, 126152.
25. Yang, S.; Saha, A.; Liang, W.; Wu, F.; Law, C.K., Extreme role of preferential diffusion in turbulent flame propagation. *Combust Flame* **2018**, 188, 498-504.
26. Zhang, M.; Wang, J.; Huang, Z., Turbulent flame structure characteristics of hydrogen enriched natural gas with CO2 dilution. *Int J Hydrogen Energ* **2020**, 45, (39), 20426-20435.
27. ASPDEN, A.J.; DAY, M.S.; BELL, J.B., Turbulence–flame interactions in lean premixed hydrogen: transition to the distributed burning regime. *J Fluid Mech* **2011**, 680, 287-320.
28. Chakraborty, N.; Cant, R.S., Effects of Lewis number on flame surface density transport in turbulent premixed combustion. *Combust Flame* **2011**, 158, (9), 1768-1787.
29. Coulon, V.; Gaucherand, J.; Xing, V.; Laera, D.; Lapeyre, C.; Poinsot, T., Direct numerical simulations of methane, ammonia-hydrogen and hydrogen turbulent premixed flames. *Combust Flame* **2023**, 256, 112933.
30. Lapenna, P.E.; Lamioni, R.; Troiani, G.; Creta, F., Large scale effects in weakly turbulent premixed flames. *P Combust Inst* **2019**, 37, (2), 1945-1952.
31. Mohan, S.; Matalon, M., Outwardly growing premixed flames in turbulent media. *Combust Flame* **2022**, 239, 111816.
32. Lamioni, R.; Lapenna, P.E.; Troiani, G.; Creta, F., Strain rates, flow patterns and flame surface densities in hydrodynamically unstable, weakly turbulent premixed flames. *P Combust Inst* **2019**, 37, (2), 1815-1822.
33. Liu, Z.; Unni, V.R.; Chaudhuri, S.; Law, C.K.; Saha, A., Local statistics of laminar expanding flames subjected to Darrieus–Landau instability. *P Combust Inst* **2021**, 38, (2), 1993-2000.
34. Ranga Dinesh, K.K.J.; Shalaby, H.; Luo, K.H.; van Oijen, J.A.; Thévenin, D., Heat release rate variations in high hydrogen content premixed syngas flames at elevated pressures: Effect of equivalence ratio. *Int J Hydrogen Energ* **2017**, 42, (10), 7029-7044.
35. Attili, A.; Lamioni, R.; Berger, L.; Kleinheinz, K.; Lapenna, P.E.; Pitsch, H.; Creta, F., The effect of pressure on the hydrodynamic stability limit of premixed flames. *P Combust Inst* **2021**, 38, (2),

1973-1981.
36. Mandilas, C.; Ormsby, M.P.; Sheppard, C.G.W.; Woolley, R., Effects of hydrogen addition on laminar and turbulent premixed methane and iso-octane–air flames. *P Combust Inst* **2007**, 31, (1), 1443-1450.
37. Hu, E.; Huang, Z.; He, J.; Zheng, J.; Miao, H., Measurements of laminar burning velocities and onset of cellular instabilities of methane–hydrogen–air flames at elevated pressures and temperatures. *Int J Hydrogen Energ* **2009**, 34, (13), 5574-5584.
38. Hu, E.; Huang, Z.; He, J.; Jin, C.; Zheng, J., Experimental and numerical study on laminar burning characteristics of premixed methane–hydrogen–air flames. *Int J Hydrogen Energ* **2009**, 34, (11), 4876-4888.
39. Okafor, E.C.; Hayakawa, A.; Nagano, Y.; Kitagawa, T., Effects of hydrogen concentration on premixed laminar flames of hydrogen–methane–air. *Int J Hydrogen Energ* **2014**, 39, (5), 2409-2417.
40. Aung, K.T.; Hassan, M.I.; Faeth, G.M., Flame stretch interactions of laminar premixed hydrogen/air flames at normal temperature and pressure. *Combust Flame* **1997**, 109, (1), 1-24.
41. Bradley, D.; Lau, A.K.C.; Lawes, M.; Smith, F.T., Flame Stretch Rate as a Determinant of Turbulent Burning Velocity. *Philosophical Transactions of the Royal Society of London. Series a: Mathematical, Physical, and Engineering Sciences* **1992**, 338, (1650), 359-387.
42. Chen, Z., On the accuracy of laminar flame speeds measured from outwardly propagating spherical flames: Methane/air at normal temperature and pressure. *Combust Flame* **2015**, 162, (6), 2442-2453.
43. Spalding, D.B.; Jain, V.K., The theory of steady laminar spherical flame propagation: Analytical solutions. *Combust Flame* **1961**, 5, 11-18.
44. Ji, C.; Qiang, Y.; Wang, S.; Xin, G.; Wang, Z.; Hong, C.; Yang, J., Numerical investigation on the combustion performance of ammonia-hydrogen spark-ignition engine under various high compression ratios and different spark-ignition timings. *Int J Hydrogen Energ* **2024**, 56, 817-827.
45. Komen, E.M.J.; Hopman, J.A.; Frederix, E.M.A.; Trias, F.X.; Verstappen, R.W.C.P., A symmetry-preserving second-order time-accurate PISO-based method. *Comput Fluids* **2021**, 225, 104979.
46. Lei, Y.; Li, Y.; Qiu, T.; Li, Y.; Wang, Y.; Zhang, C.; Liu, J.; Ding, M.; Liu, X.; Peng, G., Effects of high-pressure methane jet on premixed ignited flame in constant-volume bomb. *Energy* **2021**, 220, 119695.
47. Bradley, D.; Shehata, M.; Lawes, M.; Ahmed, P., Flame extinctions: Critical stretch rates and sizes. *Combust Flame* **2020**, 212, 459-468.
48. Gu, X.J.; Haq, M.Z.; Lawes, M.; Woolley, R., Laminar burning velocity and Markstein lengths of methane–air mixtures. *Combust Flame* **2000**, 121, (1), 41-58.